# Temporal Evolution of the Magmatic System at Tungurahua Volcano, Ecuador, detected by geodetic observations

Cyril Muller[a,b,*], Juliet Biggs[b], Susanna K. Ebmeier[c], Patricia Mothes[d], Pablo B. Palacios[d], Paul Jarrin[d], Marie Edmonds[e], Mario Ruiz[d]

[a]*Observatorio Vulcanológico y Sismológico de Costa Rica, Universidad Nacional, 2346-3000 Heredia, Costa Rica*
[b]*School of Earth Sciences, University of Bristol, Wills Memorial Building, Queen's Road, BS8 1RJ Bristol, U.K.*
[c]*School of Earth and Environment, University of Leeds, LS2 9JT, UK*
[d]*Instituto Geofísico de la Escuela Politécnica Nacional, Ladrón de Guevara E11-253, Quito, Ecuador*
[e]*~~School of~~ Earth Sciences, University of Cambridge, Downing Street, Cambridge,*

## Abstract

Changes in the pathway and timescale of magma ascent can be responsible for variations in eruptive style during long-lived eruptions, but are only documented at a small number of well-instrumented systems. Here we integrate PS-InSAR from high resolution TerraSAR-X radar imagery with continuous GPS data from 4 sites at Tungurahua volcano, Ecuador. Our results show long-term uplift between 2011-2014 associated with a continuously inflating prolate reservoir at a depth of $\sim 10$ km beneath the summit. Comparisons with eruptive flux, taking compressibility into account, suggest that during this time period slightly over half the magma supplied to the system was erupted. The observations span three distinct phases of eruption and in 2012-2013, an increase in eruptive activity was accompanied by uplift on the volcano's western flank. Similar episodes have previously been observed during large Vulcanian eruptions and we attribute them to intrusions into an area of mechanical weakness. A localised patch of subsidence mid-way up the Tungurahua's western flank is co-located with a swarm of shallow long-period seismicity and may represent a potential site for

[*]Corresponding author
*Email address:* `cyril.muller21@gmail.com` (Cyril Muller)

a development of a lateral vent. This study demonstrates that satellite geodetic techniques are capable of characterising the geodetic signature of transitions in eruptive style during long-lived andesitic eruptions although the deformation is cm-scale of steep volcanic edifices.

## 1. Introduction

The nature of volcanic eruptions is controlled by the supply rate and composition of the magma, and the geometry of the plumbing system (Sparks, 2003). Geophysical and geochemical observations, such as seismicity, surface deforma-
[5] tion and $SO_2$ flux can be used to study the patterns of magma ascent and storage and hence forecast eruptive activity (Sparks, 2003; Biggs et al., 2014; Phillipson et al., 2013). During long-lived andesitic eruptions, a major challenge is to forecast changes in behaviour, and in particular, the transition from a open system, characterised by semi-continuous eruptions and low explosivity,
[10] to a closed system, which can generate larger explosive eruptions.

Tungurahua volcano in Ecuador has been erupting since 1999 (Mothes et al., 2015), with activity varying from Strombolian to sub-Plinian. Continuous eruptive phases last from several weeks to more than a year (Hidalgo et al., 2015), with hiatuses lasting weeks to months. In this study, we use geodetic data from
[15] GPS (Global Positioning System) and InSAR (Interferometric Synthetic Aperture Radar) to detect long term and transient deformation. We apply stacking and Persistent Scatterer methods to high-resolution InSAR images acquired by the TerrSAR-X satellite between May 2011 and April 2014. We then combine this with GPS total displacements to produce a 3D velocity map. The inte-
[20] gration of the geodetic data provides a unique insight into the temporal and spatial characteristics of the deformation processes, allowing us to identify a continuously-inflating deep reservoir and an intrusion event into the edifice.

2

## 2. Tungurahua volcano

*2.1. Geological background and current activity*

Tungurahua volcano in Ecuador is a 3000m relief, active andesite stratovolcano with a summit at 5016 m above mean sea level (a.m.s.l.). It is located in the eastern Cordillera of the Ecuadorian Andes, which is bordered to the west by the ∼30-50 km wide inter-Andean valley and to the east by the Amazonian rear-arc lowlands. The edifice was built in three main constructive periods, interrupted by two flank failure events (Hall et al., 1999). The large amphitheatre on the western flank was created by the last collapse, 3000 years ago and is now filled with weak unconsolidated material (Molina et al., 2005).

The ongoing eruption started in 1999, after eight decades of inactivity. The activity is extremely variable, alternating between short hiatuses, forceful gas explosions, ash emissions and lava fountaining (Mothes et al., 2004), with 4 VEI2 events and one VEI3. The VEI3 eruption in August 2006 generated a column which rose over 16 km above sea level, pyroclastic flows that covered half of the western cone, reaching the surrounding drainages (Kelfoun et al., 2009) (Fig. 1) and ash fall of more than 10 cm on the south-western part of the edifice (Eychenne et al., 2013) (Fig. 1).

Between July 2009 and July 2014, the volcano experienced 3 distinct phases of behaviour (Hidalgo et al., 2015) (Fig. 2 and Fig. 3). The first phase, from July 2009 to November 2011, was characterized by highly explosive eruptions with well-defined starts and ends. The eruptive episodes were spaced 4 to 6 months apart, and each lasted between a month and two months. The second phase, between December 2011 and August 2012, was characterised by continuous, low-level Strombolian explosions and ended with a Vulcanian explosion on August $21^{st}$ (Mothes et al., 2015). This phase lasted 9 months and only a few days of hiatus. The third phase, from September 2012 to July 2014, was again a period with well-defined explosions and at least 5 Vulcanian eruptions. The

3

eruptions lasted between 2 weeks and a month with only one or two months
between them.

### 2.2. Geophysical and Geochemical Monitoring

Tungurahua is monitored by the Instituto Geofísico de la Escuela Politécnica
Nacional (IG-EPN), which runs seismic, tilt and GPS networks as well as a scanning differential optical absorption spectrometers (mini-DOAS) (Kumagai et al.,
2007; Palacios et al., 2015; Hidalgo et al., 2015; ?). SAR images are made freely
available through the GEO Ecuadorian Volcano Supersite (http://supersites.earthobservations.org/ecuador.php
The seimsicity is dominated by swarms of Long Period (LP) and explosion
events, which are generally correlated with eruptions (Fig. 2). Few volcano-
tectonic (VT) earthquakes are recorded, but those that do occur are mainly
located on the western flank (Palacios et al., 2015). An increase in VT events
between mid-2012 and early 2013 corresponds to the transition between the second and third phases. (Molina et al., 2005). $SO_2$ flux correlates with eruption
explosivity (Hidalgo et al., 2015), with 95% of the total emissions occurring during eruptive phases and fluxes of <100 tons per day (t/d) otherwise (Hidalgo
et al., 2015). During periods of low explosivity (e.g. November 2011 to September 2012) the average $SO_2$ flux was 700 t/d and during high explosivity phases
the flux averaged 1400 t/d. Prior to 2008, long periods of low explosivity were
the norm and the system was considered open. But after 2008, more explosive,
episodic eruptions and eruptive phases have been attributed to closed-system
behaviour (Hidalgo et al., 2015).

In 2008, InSAR detected uplift of up to 17.5 cm on the upper western flank of
Tungurahua, attributed to a sill-like intrusion within the volcanic edifice coincident with a Vulcanian eruption (Biggs et al., 2010b). Subsequently, a Persistent
Scatterer (PS) study using ENVISAT SAR data between 2003 and 2009 found
continuous uplift over a 25 km-radius area, centered on Tungurahua (Champenois et al., 2014). The deformation of up to 8 mm·y$^{-1}$ is best modelled by a
continuously replenishing reservoir seated at 11.5 km below m.s.l., or 16.5 km
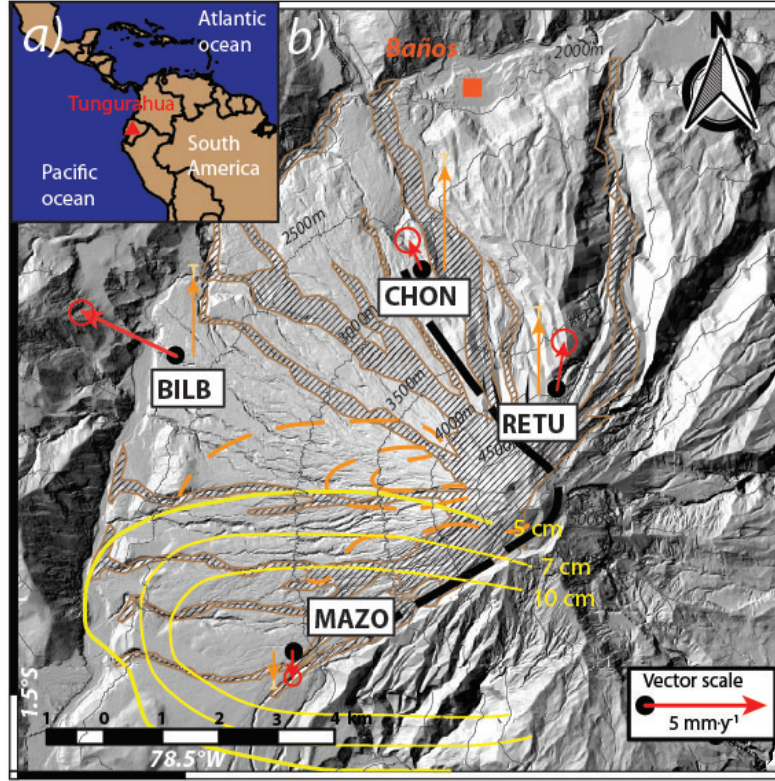
4

Figure 1: The location and geological setting of Tungurahua volcano. a) the location of Tungurahua in the western South American continent. b) Tungurahua volcano edifice, including 2006 surge deposits described by Kelfoun et al. (2009), which are indicated by the brown hatched areas. The dashed red contours are the InSAR deformation detected by Biggs et al. (2010b) in centimetres. The thick black dashed line is the surface expression of interface of the last flank failure from Hall et al. (1999). The contours of the ash fall thickness from the August 2006 eruption from Eychenne et al. (2013) are in yellow. The red and orange arrows shows the average horizontal and vertical velocities, respectively, of the GPS sites between May 2011 and March 2014 (when the TerraSAR-X imagery was acquired).
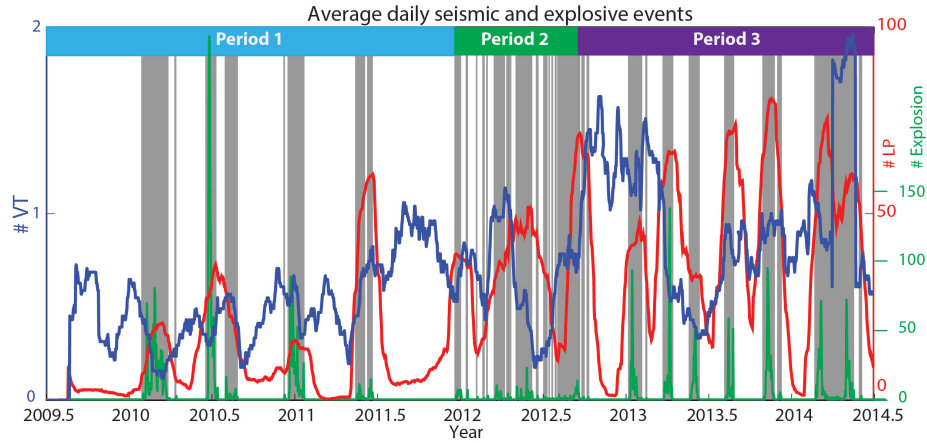
Figure 2: Daily number of Volcano-Tectonic (VT), Long Period (LP) and explosive events detected by the Instituto Geofisico seismic network. A centred moving average with a window of 50 days has been applied to the VT (blue line) and LP (red line) counts. The green line shows the number of explosions per day while the grey bars indicate days on which at least one sub-aerial explosion occurred. The three different periods with different eruptive behaviour identified by Hidalgo et al. (2015).

beneath the active crater. In contrast, petrological data from the 2006 eruption
<sup>85</sup> indicates a magma source at 8 to 10 km below the summit, equivalent to 3 to 5 km below sea level (Samaniego et al., 2011). Champenois et al. (2014) found no persistent scatterers on the edifice itself, so is insensitive to shallow sources of deformation. Short-term cycles of inflation/deflation preceding eruptions are also detected by a single tiltmeter, RETU, located within 1 km of the volcano's
<sup>90</sup> summit (**?**).

## 3. Methods

### 3.1. InSAR and StaMPS

TerraSAR-X is a right-looking X-band SAR satellite operated by the Deutsches
<sup>95</sup> Zentrum für Luft- und Raumfahrt (DLR). We use 41 images from May $13^{th}$ 2011 to March $1^{st}$ 2014. The satellite has a wavelength of 31 mm, and high spatial
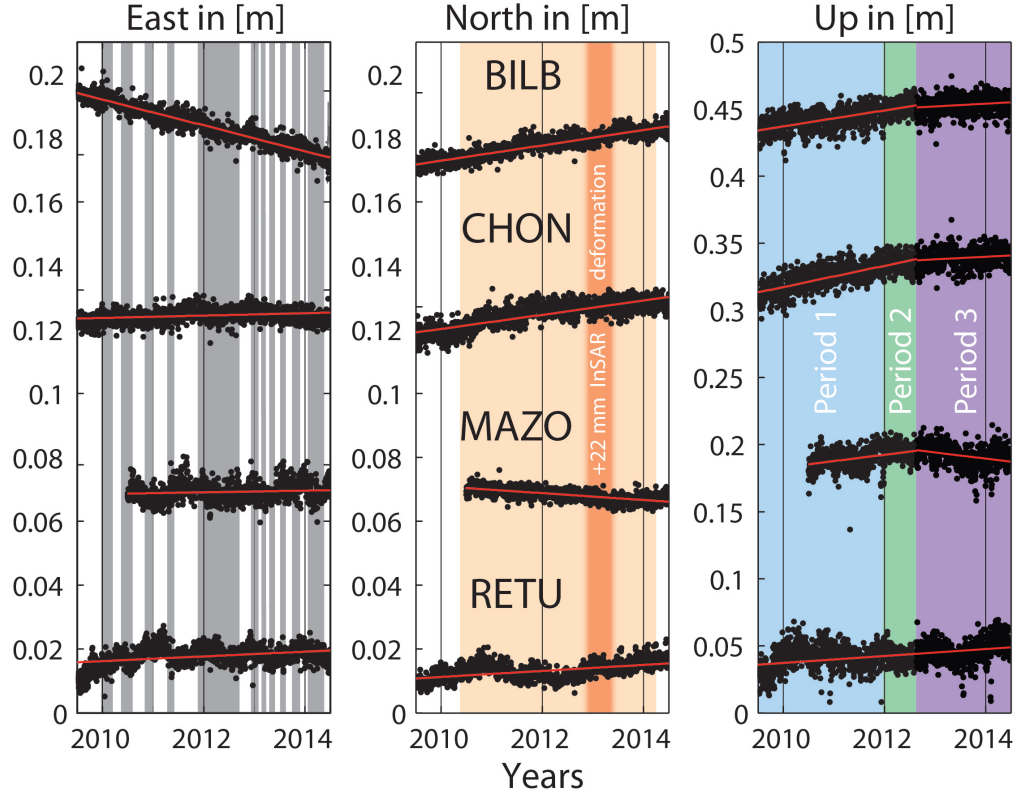
Figure 3: GPS time series from Mid-2009 to mid-2014. The black dots are the daily GPS solutions for the North, East and up components. The red lines show the trend of each time series. At the end of the second period, the vertical time series of BILB, CHON and MAZO GPS sites show a >4 mm·y$^{-1}$ change in the trend (see Results section). The East subplot, the grey rectangles denote eruptive periods from Hidalgo et al. (2015). The North subplot, the light orange rectangle show the period of InSAR acquisition while the darker orange rectangle show the period when +22 mm InSAR deformation have been detected. The Up subplot, the three different periods with different eruptive behaviour identified by Hidalgo et al. (2015).

7

resolution of 1 m, but coherence is rapidly lost in vegetated areas (e.g. Ebmeier et al., 2013). Tungurahua is a steep-sided stratovolcano, so, the western flank is better imaged by descending satellite passes and the eastern flank by ascending passes. Recent eruptive deposits cover the western flank, which is consequently less vegetated than the eastern flank. TerraSAR-X has a repeat orbit of 11 days, but intervals between successive acquisitions vary between 11 days and months depending on the satellite acquisition schedule. Interferograms were processed using the ROI-PAC software (Rosen et al., 2004) and topography was removed with a 5 m resolution Digital Elevation Model acquired from an airborne LiDAR (Light Detection And Ranging) mission ordered by IG-EPN.

Individual interferograms are dominated by stratified tropospheric noise associated with the high relief edifice (3-5 cm) (e.g. Parker et al., 2015; Ebmeier et al., 2013) so we combine interferograms to improve the signal-to-noise ratio (Biggs et al., 2010a; Berardino et al., 2002; Hooper et al., 2007). First, we stack the common coherent parts of each interferogram using the assumption that noise is random but this results in very limited spatial coverage ( Fig. 4a).

Next, we apply the Persistent Scatterer (PS) method (Hooper et al., 2007), which uses amplitude dispersion (Ferretti et al., 2001) and the stability of the phase of each pixel to select persistent scatterers which are then used for further analysis (Hooper et al., 2009; Riddick et al., 2012; Pinel et al., 2011). Firstly, the raw images and interferograms are computed relative to a common master image, and then in a series of iterations, the algorithm identifies the candidate pixels that have persistent scattering characteristics through time. The spatial correlation characteristics of the signal are then used to reduce the noise due to orbital and atmospheric errors. We chose the January $29^{th}$ 2013 acquisition as the master image because it is in the middle of our period of study. The spatial coverage is limited by the DEM rather than the SAR images. We obtain 24,541 persistent scatterers mainly located at the foot of the volcano, although a significant number are situated on the edifice itself. The root mean square
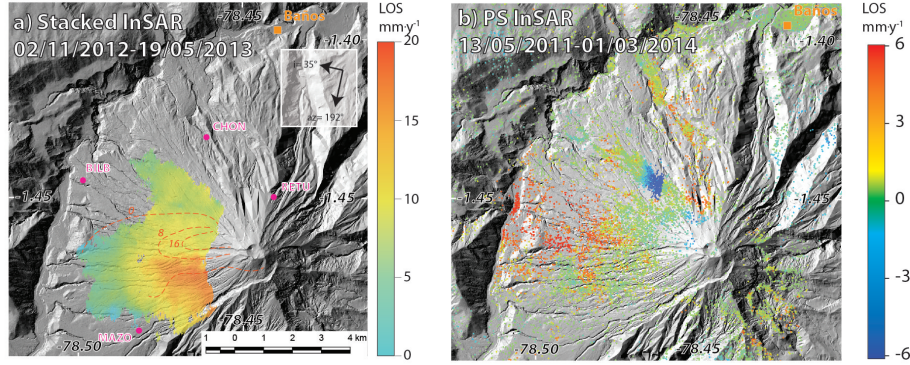
Figure 4: InSAR observations from TerraSAR-X track 142. a) displacement from stacked interferograms between November $2^{nd}$ 2012 and May $19^{th}$ 2013. The orange dashed contours show the early 2008 co-eruptive displacements in cm from Biggs et al. (2010b). Within the white box, the arrows with a value in degrees are the orbital heading and incidence angle of track 142 used for both insets. The pink dots are the 4 permanent GPS sites. b) velocities from InSAR Persistent Scatterers analysis using StaMPS for the May 2011-March 2014 period.

error (RMSE) on velocity is between 0.4 and 2.1 mm·y$^{-1}$ ( Fig. 4b).

## 3.2. Integration of GPS and InSAR

InSAR has a high spatial coverage but low temporal resolution and measures velocity only in the line-of-sight (LOS) of the satellite, while GPS measures 3 components of displacement in an absolute reference frame, but at a sparse network of sites. Combining InSAR and GPS takes advantage of the benefits of each approach, and can be used to produce a 3-D displacement or velocity field (Samsonov and Tiampo, 2006; Guglielmino et al., 2011; Muller et al., 2015).

In 2009-2010, four permanent GPS stations were installed at Tungurahua. RETU on the northern flank is at 3900 m above mean sea level (m.s.l.); MAZO and CHON on the south-western and north-western flank are at elevations of 2900 and 2800 m above m.s.l. respectively and BILB is located on the foot of the western flank at 2300 m above m.s.l.(Fig. 1). Daily positions of the GPS sites are computed with GAMIT/GLOBK software (Herring et al., 2010). The fiducial site, RIOP, located 39 km south-west of the volcano, is used to remove

9

the tectonic signal and most of the atmospheric artefacts (Fig. 3). The RMSE
of the vertical and horizontal GPS velocities is below 2 millimetre per year for
all the sites at 95% confidence.

We use the continuous medium method of Guglielmino et al. (2011) to com-
bine InSAR and GPS measurements (Guglielmino et al., 2011; Muller et al.,
2015). The 3D velocity vector, $v_P$, and gradient tensor, $\mathbf{H}$, are computed for
each pixel $P$ using: 1) the InSAR velocities $\mathbf{v_m}$ at the pixel $P$; 2) its 3D posi-
tion, $\mathbf{x_p}$ from a DEM and 3) the velocities $\mathbf{v_n}$ of the $n$ surrounding GPS sites.
The stochastic model accounts for the accuracies of each observation, weighted
according to the distance between the computed pixel $P$ and the $n$ GPS sites
as necessary.

GPS velocities are available from July 2009 whereas TerraSAR-X images
are only available from May 2011. Therefore, we use the mean velocity of
both GPS and InSAR over the May 2011-March 2014 period to generate a
integrated deformation field (Fig. 5). To downsample the InSAR, we create a
100 m x 100 m grid and compute the velocity for each pixel that contains at
least one PS. When several PS were available in the same pixel, we use their
accuracy to calculate a weighted average of the deformation rate. The InSAR
data are shifted to agree with the GPS velocities projected in the LOS velocity
to make use of the absolute reference frame provided by the GPS network,
following Muller et al. (2015). Using the average velocity from both GPS and
InSAR observations results in a temporal smoothing of the deformation which
is adequate for investigating a long-term process (e.g. replenishment of a crustal
reservoir) but not for pre-eruptive or transient processes. The root mean square
error of the integrated velocity field is $<2$ mm·y$^{-1}$.

10

Table 1: Averaged velocities for the GPS sites for the mid-2009 to mid-2014 period and when InSAR data were acquired from May 2011 to March 2014. RMS velocity errors <2 mm at 95% confidence.

| Site | July 2009 - July 2014 | | | May 2011- March 2014 | | |
|---|---|---|---|---|---|---|
| | East | North | Up | East | North | Up |
| | | | $[\text{mm}\cdot\text{y}^{-1}]$ | | | |
| BILB | -4.1 | 2.4 | 4.2 | -4.0 | 1.9 | 3.2 |
| CHON | 0.4 | 2.2 | 5.7 | -0.5 | 1.2 | 4.3 |
| MAZO | 0.4 | -1.0 | 0.5 | 0.3 | -1.2 | -1.3 |
| RETU | 0.7 | 1.0 | 1.9 | 0.3 | 2.0 | 3.1 |

## 4. Results

### 4.1. Long-term deformation (¿ 3 years)

The GPS displacement and velocity time series of all four GPS sites show both long-term trends and transient changes. The long term velocities make a radially outward pattern, with uplift at all the sites (Fig. 1) and larger rates at the base of the edifice than at the top (Tab 1, Fig. 3). The largest magnitude deformation in the StaMPS velocity field occurs at the base of the western flank and at a sharp-edged area of subsidence located on the western flank (Fig. 4b). A long wavelength gradient from motion away from the satellite on the eastern flank and movement towards the satellite on the western flank could be associated with orbital errors in the InSAR. However, GPS vertical velocities reveal the same trend and we conclude this signal is a displacement of the volcano surface.

The integrated velocity field between May 2011 and March 2014 shows i) radially outward displacement vectors across the entire edifice, which are centred 2 km to the west of the crater, ii) the northwestern third of the edifice is dominantly uplifting with larger rates at the base of the edifice than at the summit and iii) subsidence on the eastern flank (Fig. 5). The maximum uplift of  10

11

$\text{mm·y}^{-1}$ is located at the base of the edifice, close to the BILB GPS site. There are no GPS sites located on the other side of the drainage which surrounds the volcano, so the velocities in the far field have high uncertainties (label 4 in Fig 5) and we do not consider this area further.

In addition to this general pattern, we detected several deformation areas of smaller spatial coverage: on the northwestern flank, we detect a small area of subsidence (labeled 1 in Fig 5); the upper 900 m of the edifice shows subsidence of several millimetres per year (2 on Fig 5) and we observe subsidence on the eastern flank from Baños to an altitude of 4000 m (3a,b on Fig 5). The area of subsidence on the northwestern flank (labeled 1) is approximately 900m by 600 m in extent and has a sharp boundary with the surrounding area. The boundary is sharpest in the east consistent with a trap door style motion (e.g. Amelung et al., 2000).

We investigate the source parameters responsible for the large-scale, long-term uplift and radial deformation. First, we forward model the best-fit parameters from the 2003-2009 InSAR study (Champenois et al., 2014): a point source at 14.5 km below the average surface with a continuous rate of volume change of around 7 million $\text{m}^3 \text{·y}^{-1}$ (Table 2). The original model assumed the source was located directly beneath the active crater, however, our data, which include more PS points on the edifice suggests the centre of the radial pattern is 2 km further west and we adapt the model accordingly (Fig. 6). Subtracting the adapted model from our observations shows only minor residuals in the horizontal components ($<2 \text{ mm·y}^{-1}$), but vertical residuals of $>5 \text{ mm·y}^{-1}$ (Fig. 6b).

Prolate source geometries generate a greater horizontal to vertical displacements than a spherical or point source and are regarded as more physically realistic for a stratovolcano (Odbert et al., 2014). Using the programme dModels (Battaglia et al., 2013), the best-fitting prolate source has a 2 km long axis and 200 m short axis, inclined at an angle of 25 ° degrees toward the west-northwest
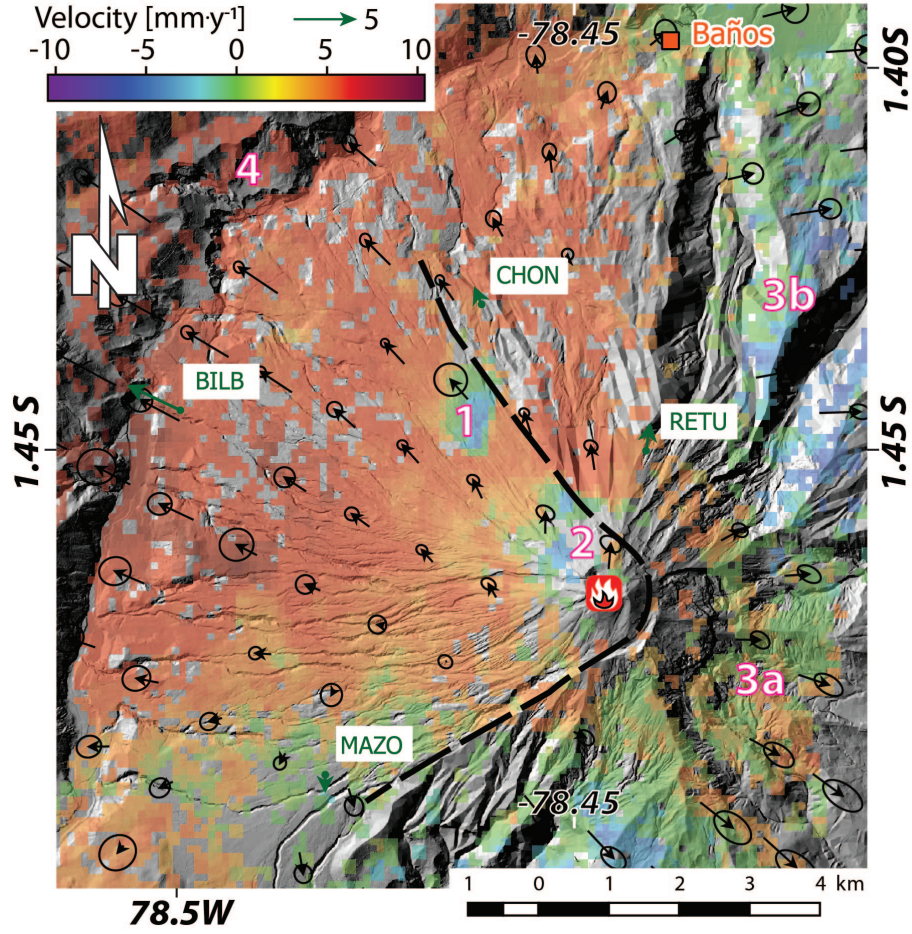
12

Figure 5: Integrated velocity field and its accuracy between May 2011 and March 2014 at Tungurahua volcano. The color map shows the vertical velocities while the black arrows display the horizontal velocity and their ellipse of accuracy. Dark green arrows represent the horizontal velocities for the 4 GPS sites. The black dashed line is the avalanche caldera scar from Hall et al. (1999).The pink and white numbers show the significant residual areas on the prolate model.

(azimuth $\phi = 300°$). The depth of 7.4 km beneath the mean elevation or 9.9 km beneath the summit (Table 2) and volume change of $\sim$2 M m$^3\cdot$y$^{-1}$, are discussed further in section 5. The prolate shape can reproduce both the horizontal and vertical patterns of deformation: the residuals of this model are <2 mm$\cdot$y$^{-1}$ in the horizontal and mainly <1 mm$\cdot$y$^{-1}$ across the edifice. This model cannot account for the small areas of subsidence described previously (1, 2, 3a and 3b in Fig. 5).

None of these models account for topography or anisotropy and need to be interpreted carefully when applied to steep-sided volcanoes such as Tungurahua which has relief of 3000 m. The half-space assumption can cause an underestimate of volume change by a factor of up to 50% (Cayol and Cornet, 1998), corresponding to an increase of 1 Mm$^3\cdot$y$^{-1}$ for our data. Anisotropy and inelastic effects may have even greater impact on the modelled volume, depth and shape of the reservoir (Trasatti et al., 2003; Gottsmann and Odbert, 2014), but few constraints exist on these parameters at Tungurahua. Therefore, we consider the modelling to be an initial first-order approach at explaining the complex displacement field.

Table 2: Parameters of the tested models. Elastic parameters of these models are 4$\cdot$10$^9$ GPa for the 1$^{st}$ Lame constant and 6.25$\cdot$10$^9$GPa for the shear modulus. $\chi^2$ is the overall misfit, unitless. The depth is measured from average elevation, 2.5 km above sea level, which is $\tilde{2}$.5 km from the summit. The center of the source is at -78.47E and -1.46N, at 2 km West from the crater.

| Parameters | Models | |
| --- | --- | --- |
| | Mogi | Prolate |
| Depth [km] | 14.5 | 7.4 |
| $\Delta$Volume [Mm$^3\cdot$y$^{-1}$] | 7 | 2 |
| Semi-major, minor axes [km] | - | 2 by 0.2 |
| Dip (0 = vertical prolate) [°] | - | 25 |
| Strike [°] | - | 300 |
| $\chi^2$ [-] | 0.7 | 0.5 |

*4.2. Medium time scale deformation (6-24 months)*

We define medium time scale deformation as transient events that occur over 6 to 24 months. By stacking the InSAR data, we detect uplift of $\sim$2 cm high on the south-western flank during the period between November $2^{nd}$ 2012 and May $19^{th}$ 2013 (Fig. 4a); with an average rate of 4 cm·y$^{-1}$. To investigate this signal further, we look for transients in both the InSAR and GPS data (Fig. 7 and Tab 3), by subtracting the long-term deformation associated with the best-fitting prolate source and subdividing the data into the three periods identified by (Hidalgo et al., 2015): a) May $13^{th}$ 2011-November $2^{nd}$ 2012 (16 SAR images); b) November $2^{nd}$ 2012-May $19^{th}$ 2013 (8 SAR images); c) May $19^{th}$ 2013-March $1^{st}$ 2014 (17 SAR images). PS points with non-linear velocities, defined as RMSE to the linear regression greater than 1 cm LOS, are disregarded. We use the GPS velocities to define the absolute reference frame for the InSAR observations, but over such short time periods it is not appropriate to formally integrate GPS and InSAR datasets.

From May 2011 to November 2012, the dominant feature is the 'trap door' on the western flank, which moved away from the satellite at a rate of $\sim$10 mm·y$^{-1}$ (label a, Fig. 7a). During the second period, November 2012 to May 2013, there was deformation of $\sim$40 mm·y$^{-1}$ towards the satellite, corresponding to a total of 22 mm in 6.5 months (label d, Fig. 7b). The deformation is centered on the western flank, mainly between 2800 m and 3600 m above sea level, consistent with that observed in the stacked InSAR but better characterised by the PS analysis (Fig. 4a). Deformation toward the satellite is also visible on the northern flank (label e, Fig. 7b) but with velocity <30 mm·y$^{-1}$. During the last period, May 2013 to March 2014, the deformation pattern is similar to the first period: with the 'trap door' moving at a rate of $\sim$10 mm·y$^{-1}$ (label f, Fig. 7c) and subsidence of $\sim$6 mm·y$^{-1}$ on the southeastern flank (label h, Fig. 7c) .

Although located outside the deforming area, the GPS sites BILB, CHON
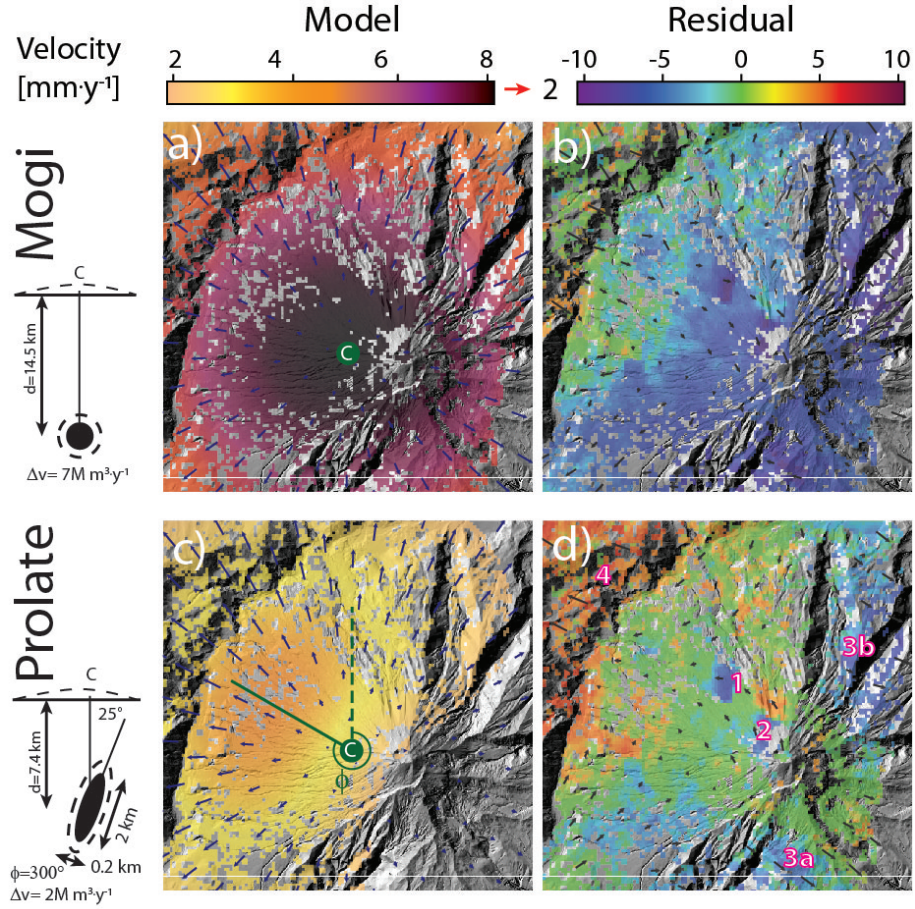
Figure 6: Results of the analytical modeling. Panels a) and b) present the predicted deformation from a Mogi model and the residual with our data. We use Champenois et al. (2014)'s parameters, but move the centre of the source westward to better fit our data. Panels c) and d) show the Yang model resulting from our best inversion. The blue arrows show the deformation implied by the models while the grey arrows show the residuals velocity vectors. The colored map shows the vertical velocities. The letter C within the green circle shows the position of the centres of the deformation source. The pink and white numbers show the significant residual areas on the prolate model.

16

Table 3: Average vertical velocities of the GPS sites and their respective RMSE for the July 2009 to July 2012 and from July 2012 then to July 2014. The trend due to the inflating prolate was subtracted from these velocities.

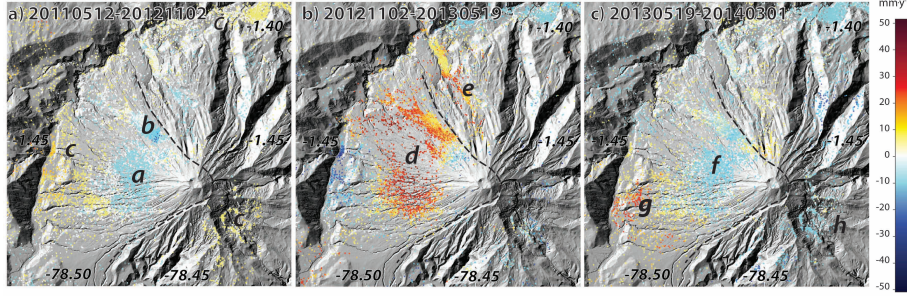| Site | July 2009-July 2012 | July 2012-July 2014 | Velocity change |
| --- | --- | --- | --- |
| | | $[\mathrm{mm}\cdot\mathrm{y}^{-1}]$ | |
| BILB | 1.3 ±2.0 | -3.7 ±4.0 | -4.6 ±4.5 |
| CHON | 1.1 ±2.8 | -5.3 ±6.3 | -6.4 ±6.4 |
| MAZO | 2.0 ±5.9 | -7.3 ±7.6 | -9.3 ±9.6 |
| RETU | -5.9 ±13.2 | -2.7 ±15.4 | +3.2 ±20.3 |



Figure 7: PS-InSAR LOS velocities for the 3 sub-periods as defined by Hidalgo et al. (2015). Positive values are deformation toward the satellite. The letters correspond to the features described in the text. The LOS velocities are referenced to the GPS sites as described by Muller et al. (2015).

and MAZO all show velocity changes in July 2012 (Fig. 3). After the long-term trend associated with the inflating prolate source is removed, the change in vertical velocity at BILB is -4.6 ±4.5 mm·y$^{-1}$, at CHON is -6.4±6.4 and at MAZO is 9.3±9.6 mm·y$^{-1}$ (Tab. 3). These changes are close to the level of significance and well below the centimetric accuracy of the PS analysis. However, the velocity change coresponds with a change in the eruptive activity reported by Hidalgo et al. (2015), and occurs shortly before the rapid uplift of the western flank seen in the InSAR (label d, Fig. 7e).

17

## 5. Discussion

<sup>280</sup> By combining InSAR and GPS data from Tungurahua volcano, Ecuador, we have identified both long-term magma flux into a mid-crustal reservoir and episodic endogenous growth within the edifice. Our results agree with previous studies (Biggs et al., 2010a; Champenois et al., 2014; Hidalgo et al., 2015) but provide a more detailed view of the temporal and spatial behaviour of the <sup>285</sup> plumbing system (Fig. 8). In this section, we discuss the implications of these results for the evolution of the magmatic system at Tungurahua, and for long-lived andesitic eruptions in general.

### 5.1. Mid-crustal magma supply and storage

<sup>290</sup> InSAR data from 2003-2009 detected inflation of a mid-crustal reservoir (Champenois et al., 2014), and our GPS-InSAR velocity field from 2011-2014 shows a similar displacement pattern. However, the inferred source models differ, with a depth of 16 km beneath the crater (14.5 km beneath the average surface) in 2003-2009 (Champenois et al., 2014) and 9.9 km beneath the crater <sup>295</sup> in 2011-2014 (this study with prolate model). Petrological methods estimate a source depth of ∼10 km for the 2006 eruption (Samaniego et al., 2011). Several plausible physical explanations exist for the inferred difference, including a change in deformation source or subsidence of the thick pyroclastic flows and fall deposits from the 2006 eruption (e.g. Borgia, 1994; Stevens et al., 2001; Ebmeier <sup>300</sup> et al., 2010; Odbert et al., 2015). However, there are also significant differences in processing strategy and coverage. The 2003-2009 study used Envisat data which has a greater spatial extent but found few permanent scatterers on the edifice (Champenois et al., 2014), whereas our 2011-2014 study uses higher resolution TerraSAR-X data which covers a smaller area (∼7km) but produced PS <sup>305</sup> points on the edifice itself. Furthermore, integrating the InSAR results with GPS produces a 3D velocity field rather than a measurement in a single line-of-sight, enabling us to estimate the ratio of horizontal and vertical motion, diagnostic of different source geometries.

a)

b) Trap door possible mechanisms

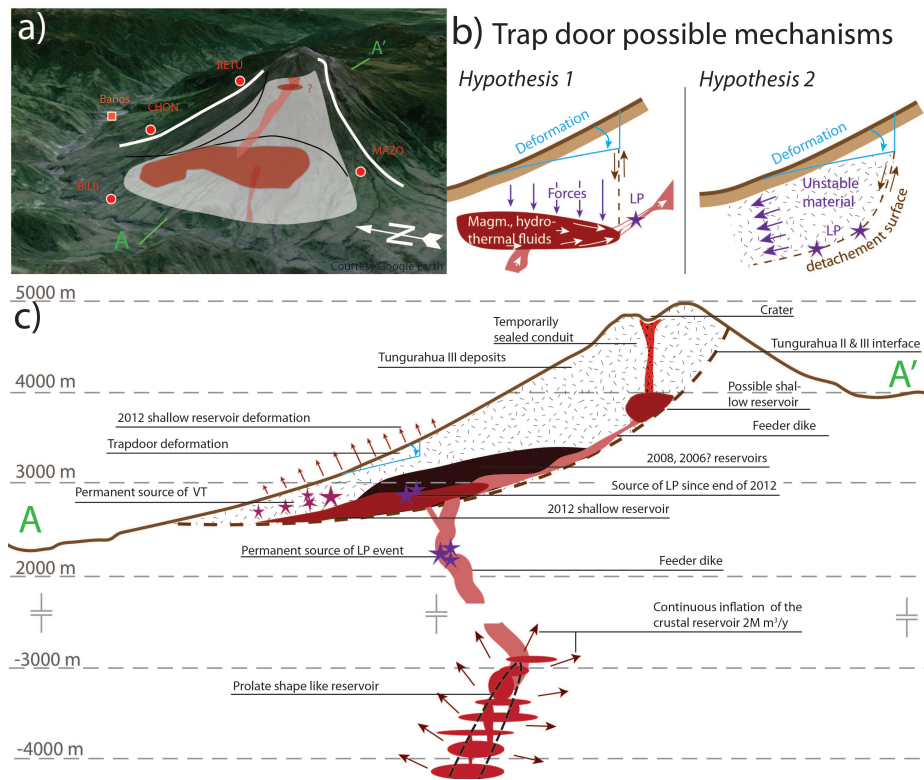Hypothesis 1

Hypothesis 2

c)

Figure 8: Proposed Tungurahua plumbing system and the time scale of its eruptive processes. a) oblique view of the volcano edifice and a global view of the current magma pathway. b) Possible mechanisms for generating the trap door subsidence c) detailed West-East cross section of the plumbing system.

The difference in modelled depth trades-off against volume change, with a
flux of 7 $Mm^3 \cdot y^{-1}$ in 2003-2009 (Champenois et al., 2014) but only 2 $Mm^3 \cdot y^{-1}$
in 2011-2014 (this study). However, the eruptive flux was also larger in 2003-
2009 at 33 $Mm^3 \cdot y^{-1}$ Dense Rock Equivalent (DRE) compared to 5 $Mm^3 \cdot y^{-1}$
DRE in 2011-2014 (Mothes et al., 2015). Although Champenois et al. (2014)
compared eruptive flux with volume change, they do not take into account
compressibility, which can cause differences in volumes of more than a factor
of 10 for large explosive eruptions (Kilbride et al., 2016). The ratio between
erupted volume and volume change at depth is:

$$\frac{V_e}{\Delta V} = -(1 + \frac{K_m}{K_c})$$ (1)

where $V_e$ is the erupted volume, $\Delta V$ the corresponding volume loss in the
crustal reservoir, $K_m$ is the magma compressibility and $K_c$ is the compressibility
of the magma reservoir (Mastin et al., 2008; Cervelli et al., 2010; Kilbride et al.,
2016). Assuming a shear modulus of 3 GPa, the chamber compressibility, $K_c$,
is $3.3 \times 10^{-10}$ $Pa^{-1}$ for a spherical chamber and $4 \times 10^{-9}$ $Pa^{-1}$ for a prolate
chamber (e.g. Kilbride et al., 2016).

To estimate the magma compressibility, $K_m$, we follow the approach of Kil-
bride et al. (2016) using ~~values of~~ 3 wt% ~~$H_2O$~~ and an oxidation state of NNO+1
based on petrological observations from the 2006 eruption (Samaniego et al.,
2011). ~~For~~ 1000 ppm $CO_2$, ~~andesitic magma~~ would be vapour undersaturated
at 10 km depth, giving $K_m = 1.5 \times 10^{-10}$ $Pa^{-1}$, whereas, ~~for~~ 5000 ppm $CO_2$,
the exsolved vapour would increase the value of $K_m$ to $2.5 \times 10^{-10}$ $Pa^{-1}$. This
gives volume ratios from 1.5 to 2, consistent with other observations from deeply
sourced, large explosive eruptions (Kilbride et al., 2016).

Table 4 gives the equivalent subsurface and erupted volumes and rates once
compressibility has been taken into account. From global observations of long-
term fluxes, the ratio of intruded to extruded magma ranges between 1 to 10,
with a mode of 2-3 and median of 5 (White et al., 2006). On shorter timescales,
this ratio will vary through the eruption cycle, with high eruptive fluxes dur-

20

Table 4: Volume balance based on observations from estimates of eruptive volume at the surface (adjusted to Dense Rock Equivalent, DRE) and reservoir volume changes from surface deformation. The values in bold are based on the observations, while values in italics are the converted values using a compensating factor for compressibility. Magma supply rate/volume is the sum of the accumulated and the erupted values. The 2003-2009 values are from Champenois et al. (2014) and Mothes et al. (2015).

| | In the crust (i.e. compressed) | At the surface (DRE) |
|---|---|---|
| *2011-2014 rates* | | |
| Accumulation rate (this study) | **2±0.5 Mm³·y⁻¹** | *3.5±0.7 Mm³·y⁻¹* |
| Eruption rate (Mothes et al., 2015) | *2.9±0.7 Mm³·y⁻¹* | **5±2.9 Mm³·y⁻¹** |
| Supply rate | 4.9±0.9Mm³·y⁻¹ | 8.5±3.0 Mm³·y⁻¹ |
| *2011-2014 volumes* | | |
| Accumulation | **6±0.9 Mm³** | *10.5±1.3 Mm³* |
| Eruption | *8.6±3.7 Mm³* | **15±5 Mm³** |
| Supply | 14.6±3.8 Mm³ | 26 ± 5.1 Mm³ |
| *2003-2009 volumes* | | |
| Accumulation | **47±? Mm³** | *82±? Mm³* |
| Eruption | *52.5±7.4 Mm³* | **105±10 Mm³** |
| Supply | 100±7.4 Mm³ | 187±10 Mm³ |

ing eruptive periods balanced by intrusion during non-eruptive periods. During the eruption at Tungurahua, we find ratios ranging from 1.7 (2011-2014) to 1.8 (2003-2009) accounting for compressibility. The magma supply rate varies between 8.5 Mm³·y⁻¹ (2011-2014) and 27 Mm³·y⁻¹ (2003-2009) which is 6 to 18 time higher than the long term rate of Tungurahua edifice growth (1.5 Mm³·y⁻¹ (Hall et al., 1999)). Assuming all the magma remains eruptible, the current supply rate (8.5 Mm³·y⁻¹) would accumulate the volume of the August 2006 sub-Plinian eruption (50-100 Mm³ (Eychenne et al., 2012; Mothes et al., 2015)) after 6-12 years.

The S0$_2$ loss during 1999-2006 period required a degassed volume of 150
Mm$^3$ DRE (Arellano et al., 2008; Hidalgo et al., 2015), which is roughly two to three times greater than predicted by extrapolating the 2011-2014 rate of magma supply over 7 years (60 Mm$^3$ DRE). Excess SO$_2$ emission is a common feature of active volcanoes, and several processes are invoked to explain this, including degassing of large bodies lying at shallow level; remobilisation of sulphur deposits and mixing between reduced and oxidized magmas (Rose et al., 1982; Witter et al., 2005; Kress, 1997). However, it is also possible that the rate of magma supply is decreasing as the eruption continues, and rates were higher for the 1999-2006 period.

### 5.2. Temporal changes in magmatic pathways

The eruption at Tungurahua is long-lived, but the pattern and characteristics of eruption are continually changing. Hidalgo et al. (2015) use the pattern of explosivity and gas flux to identify distinct phases of eruption, and here we use geodetic observations to investigate the differences in subsurface processes associated with changes in eruptive behaviour.

During period 1 (July 2009-Nov 2011), the eruptions were explosive, with high gas flux and short durations (Hidalgo et al., 2015) and the western flank subsided slowly, suggesting some of the erupted magma and/or gas was sourced from within the edifice. During period 2 (Nov 2011 to Sept 2012), the eruptive activity was characterised by low explosivity (Strombolian) and low S0$_2$ flux (Mothes et al., 2015; Hidalgo et al., 2015). However, the subsidence continued, suggesting that the change in behaviour was associated with a change in flux from deeper in the system.

Between July and December 2012, a clear transition in behavior occurred with 1) the resumption of strong episodic eruptions associated with high S0$_2$ flux and Vulcanian eruptions; 2) uplift of the western flank by 2 cm, 3) an increase in the number of VT events on the western flank (Fig 2) and 4) a decrease in vertical

22

velocity at the GPS sites. These observations are consistent with an intrusion into the western flank.

380

From December 2012 to July 2014, the volcanic activity was characterized by strong, short eruptions including 5 Vulcanian eruptions, separated by very short hiatuses showing low $SO_2$ flux Hidalgo et al. (2015). Both VT activity and co-eruptive $S0_2$ flux were high (Fig. 2) and the western flank was again

385 subsiding. We conclude that magma and/or gas from the earlier intrusion may have helped feed the eruption which is also supported by tilt meter observations (**?**).

### 5.3. Growth and deformation of the edifice

390 Although an order of magnitude smaller, the 2012 flank intrusion had a similar ~~pattern~~ to one that accompanied the 2008 eruption (Biggs et al., 2010b). The repeated intrusions are likely exploiting a 3000 year old collapse scar on the western flank (Hall et al., 1999), which now presents a mechanical contrast between pre-collapse consolidated volcanic rock and recent deposits. Further-

395 more, the unconsolidated deposits above are characterized by low P-wave velocities Molina et al. (2005)) and likely amplify the signal further. We speculate that similar intrusions may have taken place during past periods of activity (e.g. 2003-2004, 2006), although geodetic measurements do not exist.

Both 2008 and 2012 intrusions followed long period of low but continuous activi-

400 ty, and culminated in a Vulcanian eruption (Biggs et al., 2010b; Mothes et al., 2015). In many ways, they are small-scale analogues of the cryptodome that formed prior to the eruption of Mt St Helens in 1980 (Dzurisin (2006), subsection 1.1.4). The geodetic observations alone cannot determine whether the intrusion represents shallow magma storage prior to a large eruption, or merely

405 reflects an overall increase in magma pressure within the system. The edifice is likely to be heavily fractured and will behave inelastically (Fig. 8c) (Hildreth and Wilson, 2007; Wotzlaw et al., 2014) suggesting permanent intrusion rather

23

than temporary magma storage. In either scenario, the deformation generated has significant value from a monitoring perspective, but whether an intrusion into Tungurahua's western flank could cause a collapse similar to that observed in the 1980 eruption of Mt St Helens remains to be seen.

Shallow deformation occurs on three other parts of Tungurahua's edifice, labelled 1, 2, 3a and 3b on Figure 5 and 6. The localised 'trap door' deformation pattern in the centre of the western flank (label 1 on Figure 5 and 6) occurs in a remote area, where no *in situ* observations have yet been made. However, during the August 2006 eruption, several LP events, traditionally considered to indicate fluid movement, were located at a depth of just 500 m immediately beneath this area (Palacios et al., 2015). Fluids, whether magmatic or hydrothermal, can generate trap door-like deformation by applying differential stresses during restricted circulation or emptying (e.g. Amelung et al., 2000) (Fig. 8b). Alternatively, LP events can be caused by creep within an inelastic medium (Bean et al., 2014) and the 'trap-door' deformation could be the surface expression of a rotational detachment (e.g. Ruch et al., 2010). We estimate the depth of the listric failure plane to be on the order of hundreds of meters (Dula Jr, 1991), corresponding to the depth of the LP events. In either case, this feature may indicate a potential site for lateral eruptions and hence future hazards for the downstream communities.

Subsidence NW of the active crater (label 2 in Fig 5) affects the top 900 m of Tungurahua's edifice and may be associated with the surface response to the loading of the recently erupted material, as observed elsewhere (e.g. Lu and Dzurisin, 2014; Ebmeier et al., 2014; Muller et al., 2015). Subsidence on the north-eastern and the southern flank (label 3a and 3b), is constrained by a few PS, and may be related to localised slope instabilities in unvegetated area.

## 6. Conclusion

This study combines high-resolution InSAR and GPS at Tungurahua Volcano Ecuador between 2011 and 2014. The combination of InSAR and GPS

24

produces a 3-D displacement field in an absolute reference frame which ~~en-ables~~ us to investigate the source geometry of the deep reservoir in more detail than previous studies. An asymmetric deformation pattern with a high ratio

of horizontal to vertical motion favours a tilted prolate ellipsoid located ∼7.5 km beneath the average surface. We compare the rate of accumulation within the edifice to that of eruption, accounting for magma compressibility, and find that during this period, slightly more than half of the magma supplied to the reservoir reached the surface.

The use of high resolution TerraSAR-X data with Persistent Scatterer methods enables us to study deformation of the edifice itself, and we detect an intrusion into the western flank, similar to the one that occurred during the 2008 eruption (Biggs et al., 2010b), but smaller in magnitude. The intrusions occur within the edifice, likely along the collapse scar between consolidated volcanic rock and recent deposits. Both intrusions accompanied Vulcanian eruptions and changes in eruptive behaviour, suggesting they may be useful indicators of changes in the magmatic system. We also detect a localised area of subsidence around 3300 m above sea level, that corresponds to the location of shallow long period seismicity, and may represent a potential lateral vent site.

These observations have implications for the understanding of the plumbing systems of long-lived stratovolcano eruptions such as Tungurahua, Ecuador, with consequences for short-term hazard assessments. In particular, we demonstrate the advantages of statistical methods for improving the signal to noise ratio of both InSAR and GPS data, integration of multiple geodetic datasets and comparisons with other monitoring information.

### Acknowledgments

## References

Amelung, F., Jónsson, S., Zebker, H., Segall, P., 2000. Widespread uplift and trapdoor faulting on Galapagos volcanoes observed with radar interferometry. Nature 407, 993–996.

Arellano, S., Hall, M., Samaniego, P., Le Pennec, J.L., Ruiz, A., Molina, I., Yepes, H., 2008. Degassing patterns of Tungurahua volcano (Ecuador) during the 1999–2006 eruptive period, inferred from remote spectroscopic measurements of $SO_2$ emissions. Journal of Volcanology and Geothermal Research 176, 151–162.

Battaglia, M., Cervelli, P.F., Murray, J.R., 2013. Modeling crustal deformation near active faults and volcanic centers: a catalog of deformation models. US Geological Survey Techniques and Methods , 13–B1.

Bean, C.J., De Barros, L., Lokmer, I., Métaxian, J.P., OBrien, G., Murphy, S., 2014. Long-period seismicity in the shallow volcanic edifice formed from slow-rupture earthquakes. Nature geoscience 7, 71–75.

Berardino, P., Fornaro, G., Lanari, R., Sansosti, E., 2002. A new algorithm for surface deformation monitoring based on small baseline differential SAR interferograms. Geoscience and Remote Sensing, IEEE Transactions on 40, 2375–2383.

Biggs, J., Ebmeier, S., Aspinall, W., Lu, Z., Pritchard, M., Sparks, R., Mather, T., 2014. Global link between deformation and volcanic eruption quantified by satellite imagery. Nature Communications 5:3471.

Biggs, J., Lu, Z., Fournier, T., Freymueller, J.T., 2010a. Magma flux at Okmok volcano, Alaska, from a joint inversion of continuous GPS, campaign GPS, and

interferometric synthetic aperture radar. Journal of Geophysical Research: Solid Earth 115.

Biggs, J., Mothes, P., Ruiz, M., Amelung, F., Dixon, T., Baker, S., Hong, S.H., 2010b. Stratovolcano growth by co-eruptive intrusion: The 2008 eruption of Tungurahua Ecuador. Geophysical Research Letters 37, L21302. doi:`10.1029/2010GL044942`.

Borgia, A., 1994. Dynamic basis of volcanic spreading. Journal of Geophysical Research: Solid Earth 99, 17791–17804.

Cayol, V., Cornet, F.H., 1998. Effects of topography on the interpretation of the deformation field of prominent volcanoes: Application to Etna. Geophysical Research Letters 25, 1979–1982.

Cervelli, P.F., Fournier, T.J., Freymueller, J.T., Power, J.A., Lisowski, M., Pauk, B.A., 2010. Geodetic constraints on magma movement and withdrawal during the 2006 eruption of Augustine volcano. U.S. Geological Survey Professional Paper 415, 427–452.

Champenois, J., Pinel, V., Baize, S., Audin, L., Jomard, H., Hooper, A., Alvarado, A., Yepes, H., 2014. Large-scale inflation of Tungurahua volcano (Ecuador) revealed by Persistent Scatterers SAR interferometry. Geophysical Research Letters 41, 5821–5828.

Dula Jr, W.F., 1991. Geometric models of listric normal faults and rollover folds (1). AAPG Bulletin 75, 1609–1625.

Dzurisin, D., 2006. Volcano Deformation, Geodetic monitoring techniques. Springer-Verlag Berlin Heidelberg New York, USA.

Ebmeier, S., Biggs, J., Mather, T., Amelung, F., 2013. Applicability of InSAR to tropical volcanoes: insights from Central America. Geological Society, London, Special Publications 380, 15–37.

Ebmeier, S., Biggs, J., Mather, T., Wadge, G., Amelung, F., 2010. Steady downslope movement on the western flank of Arenal volcano, Costa Rica. Geochemistry, Geophysics, Geosystems 11.

Ebmeier, S.K., Biggs, J., Muller, C., Avard, G., 2014. Thin-skinned mass-wasting responsible for widespread deformation at Arenal volcano. Frontiers in Earth Science 2, 35.

Eychenne, J., Le Pennec, J.L., Ramón, P., Yepes, H., 2013. Dynamics of explosive paroxysms at open-vent andesitic systems: High-resolution mass distribution analyses of the 2006 Tungurahua fall deposit (Ecuador). Earth and Planetary Science Letters 361, 343–355.

Eychenne, J., Le Pennec, J.L., Troncoso, L., Gouhier, M., Nedelec, J.M., 2012. Causes and consequences of bimodal grain-size distribution of tephra fall deposited during the August 2006 Tungurahua eruption (Ecuador). Bulletin of Volcanology 74, 187–205.

Ferretti, A., Prati, C., Rocca, F., 2001. Permanent scatterers in SAR interferometry. Geoscience and Remote Sensing, IEEE Transactions 39, 8–20.

Gottsmann, J., Odbert, H., 2014. The effects of thermomechanical heterogeneities in island arc crust on time-dependent pre-eruptive stresses and the failure of an andesitic reservoir. Journal of Geophysical Research: Solid Earth 119, 4626–4639.

Guglielmino, F., Bignami, C., Bonforte, A., Briole, P., Obrizzo, F., Puglisi, G., Stramondo, S., Wegmüller, U., 2011. Analysis of satellite and in situ ground deformation data integrated by the SISTEM approach: The April 3, 2010 earthquake along the Pernicana fault (Mt. Etna-Italy) case study. Earth and Planetary Science Letters 312, 327–336.

Hall, M., Robin, C., Beate, B., Mothes, P., Monzier, M., 1999. Tungurahua volcano, Ecuador: structure, eruptive history and hazards. Journal of Vol-

28

canology and Geothermal Research 91, 1–21. doi:{`10.1016/S0377-0273(99)`
`00047-5`}.

Herring, T., King, R., McClusky, S., 2010. GAMIT Reference Manual, GPS
Analysis at MIT. 10.4 ed. Department of Earth, Atmospheric, and Planetary
Sciences Massachusetts Institute of Technology.

Hidalgo, S., Battaglia, J., Arellano, S., Steele, A., Bernard, B., Bourquin, J.,
Galle, B., Arrais, S., Vásconez, F., 2015. SO$_2$ degassing at Tungurahua
volcano (Ecuador) between 2007 and 2013: transition from continuous to
episodic activity. Journal of Volcanology and Geothermal Research .

Hildreth, W., Wilson, C.J., 2007. Compositional zoning of the Bishop Tuff.
Journal of Petrology 48, 951–999.

Hooper, A., Pedersen, R., Sigmundsson, F., 2009. Constraints on magma intru-
sion at Eyjafjallajökull and Katla volcanoes in Iceland, from time series SAR
interferometry. The VOLUME Project–Volcanoes: Understanding Subsurface
Mass Movement. Dublin: University College , 13–24.

Hooper, A., Segall, P., Zebker, H., 2007. Persistent scatterer interferometric
synthetic aperture radar for crustal deformation analysis, with application to
Volcán Alcedo, Galápagos. Journal of Geophysical Research: Solid Earth 112,
B07407. doi:`doi:10.1029/2006JB004763`.

Kelfoun, K., Samaniego, P., Palacios, P., Barba, D., 2009. Testing the suitability
of frictional behaviour for pyroclastic flow simulation by comparison with
a well-constrained eruption at Tungurahua volcano (Ecuador). Bulletin of
Volcanology 71, 1057–1075.

Kilbride, B.M., Edmonds, M., Biggs, J., 2016. Observing eruptions of gas-rich
compressible magmas from space. Nature Communications 7.

Kress, V., 1997. Magma mixing as a source for Pinatubo sulphur. Nature 389,
591–593.

29

Kumagai, H., Yepes, H., Vaca, M., Caceres, V., Naga, T., Yokoe, K., Imai, T., Miyakawa, K., Yamashina, T., Arrais, S., et al., 2007. Enhancing volcano-monitoring capabilities in ecuador. Eos, Transactions American Geophysical Union 88, 245–246. doi:`10.1029/2007EO230001`.

Lu, Z., Dzurisin, D., 2014. InSAR imaging of Aleutian volcanoes: monitoring a volcanic arc from space. Springer Science & Business Media, Berlin Germany.

Mastin, L.G., Roeloffs, E., Beeler, N.M., Quick, J.E., 2008. Constraints on the size, overpressure, and volatile content of the Mount St. Helens magma system from geodetic and dome-growth measurements during the 2004-2006+ eruption. US Geological Survey Professional Paper 1750, 461–488.

Molina, I., Kumagai, H., Le Pennec, J.L., Hall, M., 2005. Three-dimensional p-wave velocity structure of tungurahua volcano, ecuador. Journal of Volcanology and Geothermal Research 147, 144–156.

Mothes, P., Hall, M.L., Samaniego, P., Ramn, P., Molina, C.L., Yepes, H., Le Pennec, J.L., Ruiz, G., Andrade, D., Enriquez, W., Garcia, A., Eissen, J.P., Hidalgo, S., Monzier, M., 2004. Monitoring of a drawn-out episodic eruption, Tungurahua volcano, Ecuador. IAVCEI General Assembly, Pucon, Chile .

Mothes, P.A., Yepes, H.A., Hall, M.L., Ramón, P.A., Steele, A.L., Ruiz, M.C., 2015. The scientific–community interface over the fifteen-year eruptive episode of Tungurahua Volcano, Ecuador. Journal of Applied Volcanology 4, 1–15.

Muller, C., del Potro, R., Biggs, J., Gottsmann, J., Ebmeier, S.K., Guillaume, S., Cattin, P.H., Van der Laat, R., 2015. Integrated velocity field from ground and satellite geodetic techniques: application to Arenal volcano. Geophysical Journal International 200, 863–879.

Neuberg, J.W., Collinson, A.S., Mothes, P.A., Ruiz, M.C., Aguaiza, S., 2018. Understanding cyclic seismicity and ground deformation patterns at volca-

30

noes: Intriguing lessons from tungurahua volcano, ecuador. Earth and Planetary Science Letters 482, 193–200.

Odbert, H., Taisne, B., Gottsmann, J., 2015. Deposit loading and its effect on co-eruptive volcano deformation. Earth and Planetary Science Letters 413, 186–196.

Odbert, H.M., Ryan, G.A., Mattioli, G.S., Hautmann, S., Gottsmann, J., Fournier, N., Herd, R.A., 2014. Volcano geodesy at the Soufrière Hills Volcano, Montserrat: a review. Geological Society, London, Memoirs 39, 195–217.

Palacios, P., Kendall, J.M., Mader, H., 2015. Site effect determination using seismic noise from Tungurahua volcano (Ecuador): implications for seismo-acoustic analysis. Geophysical Journal International 201, 1084–1100.

Parker, A.L., Biggs, J., Walters, R.J., Ebmeier, S.K., Wright, T.J., Teanby, N.A., Lu, Z., 2015. Systematic assessment of atmospheric uncertainties for InSAR data at volcanic arcs using large-scale atmospheric models: Application to the Cascade volcanoes, United States. Remote Sensing of Environment 170, 102–114.

Phillipson, G., Sobradelo, R., Gottsmann, J., 2013. Global volcanic unrest in the 21st century: an analysis of the first decade. Journal of Volcanology and Geothermal Research 264, 183–196.

Pinel, V., Hooper, A., De la Cruz-Reyna, S., Reyes-Davila, G., Doin, M., Bascou, P., 2011. The challenging retrieval of the displacement field from InSAR data for andesitic stratovolcanoes: Case study of Popocatepetl and Colima Volcano, Mexico. Journal of Volcanology and Geothermal Research 200, 49–61.

Riddick, S., Schmidt, D., Deligne, N., 2012. An analysis of terrain properties and the location of surface scatterers from persistent scatterer interferometry. ISPRS Journal of Photogrammetry and Remote Sensing 73, 50–57.

31

Rose, W., Stoiber, R., Malinconico, L., 1982. Eruptive gas compositions and fluxes of explosive volcanoes: budget of S and Cl emitted from Fuego volcano, Guatemala, in: Andesites. Wiley New York, NY, pp. 669–676.

Rosen, P.A., Hensley, S., Peltzer, G., Simons, M., 2004. Updated repeat orbit interferometry package released. Eos, Transactions American Geophysical Union 85, 47–47.

Ruch, J., Acocella, V., Storti, F., Neri, M., Pepe, S., Solaro, G., Sansosti, E., 2010. Detachment depth revealed by rollover deformation: An integrated approach at Mount Etna. Geophysical Research Letters 37.

Samaniego, P., Le Pennec, J.L., Robin, C., Hidalgo, S., 2011. Petrological analysis of the pre-eruptive magmatic process prior to the 2006 explosive eruptions at Tungurahua volcano (Ecuador). Journal of Volcanology and Geothermal Research 199, 69–84.

Samsonov, S., Tiampo, K., 2006. Analytical optimization of a DInSAR and GPS dataset for derivation of three-dimensional surface motion. Geoscience and Remote Sensing Letters, IEEE 3, 107–111.

Sparks, R., 2003. Forecasting volcanic eruptions. Earth and Planetary Science Letters 210, 1–15.

Stevens, N., Wadge, G., Williams, C., 2001. Post-emplacement lava subsidence and the accuracy of ERS InSAR digital elevation models of volcanoes. International Journal of Remote Sensing 22, 819–828.

Trasatti, E., Giunchi, C., Bonafede, M., 2003. Effects of topography and rheological layering on ground deformation in volcanic regions. Journal of Volcanology and Geothermal Research 122, 89–110.

White, S.M., Crisp, J.A., Spera, F.J., 2006. Long-term volumetric eruption rates and magma budgets. Geochemistry, Geophysics, Geosystems 7. doi:`doi:10.1029/2005GC001002`.

Witter, J., Kress, V., Newhall, C., 2005. Volcán Popocatépetl, Mexico. Petrology, magma mixing, and immediate sources of volatiles for the 1994–present eruption. Journal of Petrology 46, 2337–2366.

Wotzlaw, J.F., Bindeman, I.N., Watts, K.E., Schmitt, A.K., Caricchi, L., Schaltegger, U., 2014. Linking rapid magma reservoir assembly and eruption trigger mechanisms at evolved yellowstone-type supervolcanoes. Geology 42, 807–810.